ACS Catalysis

pubs.acs.org/acscatalysis Research Article

PdCu Electrocatalysts for Selective Nitrate and Nitrite Reduction to Nitrogen

Jeonghoon Lim, Yu Chen, David A. Cullen, Seung Woo Lee,* Thomas P. Senftle,* and Marta C. Hatzell*

Cite This: *ACS Catal.* 2023, 13, 87−98 Read Online

ACCESS | Metrics & More | Article Recommendations | Supporting Information

ABSTRACT: Electrocatalytic conversion of nitrate in waste can enable efficient waste remediation (NO_3^- to N_2) or waste valorization (NO_3^- to NH_4^+) depending on the selectivity of the catalyst. Palladium and copper electrocatalysts typically exhibit ideal nitrate and nitrite binding properties, allowing for effective destruction of nitrate. However, rational steering of selectivity through material design remains a critical challenge for PdCu electrocatalyst. Here, we use the electrochemical underpotential deposition method to synthesize palladium nanocube electrocatalysts with controlled copper surface coverage (e.g., partial and full copper coatings). We then examine the potential for NO_3^- destruction (conversion) and NO_2^- reduction reaction. We identify that partial copper-coated Pd nanocubes not only effectively facilitate the reduction of 95% of NO_3^- but also increase the reduction of NO_2^- to N_2 with 89% selectivity over 20 consecutive cycles (80 h). We also show that under these conditions, the Pd(100) surface facet is exposed. Complete copper-covered Pd nanocubes effectively facilitate the reduction of ∼99% of NO_3^-. Complete coverage of copper; however, prevented exposure of Pd(100) surface facet, promoting the selective reduction of NO_2^- to NH_4^+ with a 70% selectivity over 20 consecutive cycles (80 h). Density functional theory (DFT) calculations show that NO_3^- and NO_2^- adsorb more strongly on the Cu(100) surface compared to the Pd(100) surface, while the NO* intermediate generated from NO_3^- or NO_2^- reduction adsorbs more strongly on the Pd surface. Barrier calculations show that NO* can readily migrate from the Cu domain to the Pd domain and that the N−N coupling barrier on Pd is significantly diminished at high NO* coverage. Together, these results suggest that the high N_2 selectivity observed on the PdCu electrocatalyst is caused by the spillover of NO* from the Cu domains to the Pd domains.

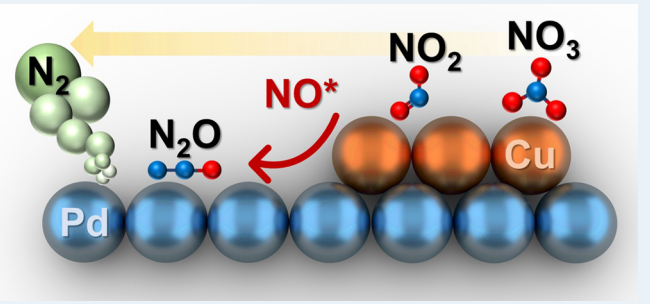

KEYWORDS: *Nitrate reduction, Nitrite reduction, Nanocrystal, Electrocatalysis, Palladium*

INTRODUCTION

Nitrate is the most widespread groundwater contaminant worldwide.[1,2] Nitrate exposure results in methemoglobinemia (blue baby syndrome) and can cause several types of cancer (gastric, colorectal, bladder, urothelial, and brain).[3] These public health impacts promote the regulation of nitrate in drinking water and wastewater. Today, the maximum contaminant levels for drinking water (MCL) are 10 ppm of NO_3^-−N and 0.3 ppm of NO_2^-−N.[4] Nearly all nitrate removal technologies for drinking and wastewater treatment rely on biological nitrification-denitrification (BND) or physicochemical separations (e.g., reverse osmosis, ion exchange resins, and electrodialysis). Biological treatment effectively converts nitrate to nitrogen gas. This is effective but energy-intensive (5−15 kWh/kg N) and expensive (approximately 10 $/kg N).[5] Conversely, physiochemical nitrate separation technologies form a brine rich in nitrates. The volume of brine produced can be equal to 1−5% of the volume of water treated. This results in high operating and maintenance costs, which are often 10−20 times the capital cost.[6] The high disposal cost is due to the brine being labeled as hazardous waste.

Catalytic conversion of nitrate from a feedstream (e.g., groundwater or wastewater) or exhaust brine could enable a more affordable solution for nitrate remediation (nitrate to nitrogen) of valorization (nitrate to ammonium). The thermocatalytic conversion of nitrate to nitrogen occurs mainly in Pd associated with In or Cu on supporting oxide materials, such as Al_2O_3, TiO_2, and SiO_2 as typical catalysts. One major drawback of catalytic conversion for nitrate removal is that thermal catalytic reduction requires additional hydrogen sources as the reducing agent. Furthermore, deactivation of the catalyst by irreversible oxidation and reduction between

Received: October 1, 2022
Revised: November 27, 2022
Published: December 12, 2022

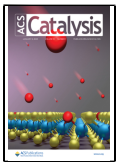

https://doi.org/10.1021/acscatal.2c04841
ACS Catal. 2023, 13, 87−98

the catalyst and the support is a serious challenge.[7] This induced the failure of the use of catalysts for large-scale water treatment. Above all, the cost of catalyst systems and electrically generated H_2 requires an additional cost $1.80 for treatment of 1 m^3 of water containing 100 mg L^{-1} pollutant.[8]

Alternatively, the electrocatalytic conversion of nitrate to nitrogen or ammonium is an attractive strategy that can be easily integrated with renewable energy. The process does not require chemical addition and thus requires operating costs lower than those of thermal routes.[9] Electrochemical denitrification is dependent on pH influence, such as changing applied potentials, atomic orientation, and adatom contribution. The pH values indicate the hydrogen species in the electrolyte, and the hydrogen adsorption kinetics is much faster than that of nitrate adsorption, resulting in a drop in the activity and selectivity at the lower pH. The selective reduction of nitrate to nitrogen occurs widely in the Pd electrocatalyst[10−12] and Pt,[13−16] which are the most N_2 selective catalyst. Controlling the structural shape and exposed facets may maximize N_2 selectivity. However, Pd does not efficiently convert nitrate to nitrite, often limiting the production rate.[17,18] Despite the low reaction rate, Pd still has promise for the electrochemical reduction of nitrate, as these metals are stable against poisoning. Strong adsorption of N intermediate species on other metals is known to poison the catalytic surface and inhibit long-term operations.[19] To overcome the limitation of the rate of Pd, while maintaining the stability of the electrocatalyst, secondary promoter metals (Cu, Sn, In) are added to Pd. Electrochemically deposited Pd−Sn bimetals on a stainless steel mesh catalyst showed an efficiency of 88% nitrate removal and a selectivity of 89% N_2. The controlled crystal structure (420) surface of the bimetallic electrodes produced the most nitrogen with a further enhancement of electrochemical nitrate reduction.[20] The nanostructured PdCu/C catalysts produced 67.8% N_2 while Pd/C produced almost 100% H_2. The presence of Cu prohibited the process associated with HER.[21] The synergistic cooperation of Cu−Pd bimetals in reduced graphene oxide (rGO) maximized the conversion of nitrate (96.7%) with the high N_2 selectivity (85.5%) due to finely anchored PdCu nanoparticles in a highly conductive rGO support.[22]

Cu is the promising material capable of suppressing hydrogen adsorption. Thus, the addition of Cu as a secondary adatom on Pd can aid in suppressing hydrogen evolution. The synergistic effect between Cu and Pd has shown a high NO_3^- conversion.[23−26] A higher composition of Pd in the bimetallic system of PdCu could produce more N_2. Maximum activity has been reported at pH 9 for the Pd−Cu catalysts.[3] In addition, the Cu(100) surface has been hypothesized to facilitate the initial steps of NO_3^- reduction, and the existence of Pd(100) improves the selectivity to N_2.[23] A selectivity transition could occur from NH_3 to N_2 due to alloying with Pd metals.[27] From a stability point of view, hydrogenated Pd stabilizes the oxidized Cu during electrolysis; thus bimetallic electrocatalysts of PdCu are an ideal combination for long-term operations.[23,27] In this study, we desire to investigate the Cu adatom on Pd(100) sites at neutral pH.

Controlling Cu coverage at the Pd sites is critical to achieve high NO_3RR activity and high selectivity toward N_2 or NH_3. Researchers have focused on the development of highly active and selective catalysts for denitrification, and reported surface modifications on Pt electrodes.[16,28−33] However, examination of the use of secondary metals in shape-controlled nanoparticles is rare.[34−36] Therefore, here we propose to focus on a strategy to incorporate Cu atoms into the surface of the Pd nanocube to achieve more efficient NO_3RR activity and high selectivity toward N_2. In this case, the Cu atoms mainly promote the initial reductions of NO_3^- and the Pd(100) facet steers the selectivity toward N_2. Here, we develop fully covered Cu atoms and partially covered Cu atoms on the surface of Pd nanocubes to investigate their electrocatalytic behaviors toward NO_3^- conversion, selectivity, and long-term stability.

RESULTS AND DISCUSSION

Engineered PdCu Electrocatalyst. We first prepared Pd nanocubes (Pd NC) as a cornerstone and reference catalyst. The UPD method was then used to prepare fully coated Cu on Pd nanocubes (f-Cu Pd NC), and partially coated Cu on Pd nanocubes (p-Cu Pd NC) (Figure 1). Two obvious reduction/

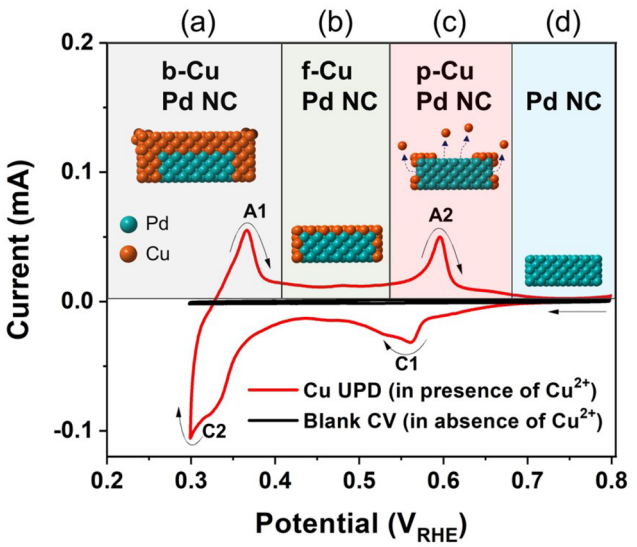

Figure 1. Electrochemical behavior of Cu bulk deposition/dissolution (C2/A1) and Cu underpotential deposition/desorption (C1/A2) on Pd nanocube/C. The CV curves were obtained in the absence and presence of Cu^{2+} in Ar-saturated 0.1 M $HClO_4$ electrolyte with a scan rate of 5 mV s^{-1}. (a) Bulk Cu on Pd NC (b-Cu Pd NC), (b) fully covered Cu on Pd NC (f-Cu Pd NC), (c) partially covered Cu on Pd NC (p-Cu Pd NC), and (d) Pd NC.

oxidation peaks (C1, C2, A1, and A2) arise during a cyclic voltammogram (CV) in the presence of Cu^{2+}. We converted all of the potentials to the reversible hydrogen electrode (RHE). The first cathodic peak (C1) when starting the scan at 0.8 V_{RHE} appeared at 0.57 V_{RHE} (Figure 1). This peak results in partial underdepositions of Cu atoms on the surface of Pd nanocubes. A second larger cathodic peak (C2) appeared at 0.3 V_{RHE}. This peak results in a Cu bulk deposition. Here, Cu coats the surface of the nanocube, forming multiple layers. Two cathodic peaks (C1 and C2) are distinguished as Cu underpotential deposition and Cu bulk deposition regions. This agrees with previous experimental and theoretical investigations.[37,38]

After bulk Cu deposition at 0.3 V_{RHE} (C2), an oxidative scan dissolves Cu from the deposited Cu multilayers (Figure 1a). The first anodic peak (A1) around 0.35 V_{RHE} helps dissolve bulk Cu, resulting in fully covered Cu atoms on the surface of Pd nanocubes (Figure 1b). Continuing the anodic scan results in a second peak (A2) around 0.6 V_{RHE} (Figure 1c). The

https://doi.org/10.1021/acscatal.2c04841
ACS Catal. 2023, 13, 87−98

additional anodic stripping results in the formation of a partial deposition of Cu on the well-defined Pd(100) nanocube facets. After the second anodic peak (A2), the Pd nanocube does not contain Cu atoms (Figure 1d).

Control over the amount of Cu atoms removed is possible through tuning the scan-rate end applied potentials. The metal desorption area at the second anodic peak (A2) provides quantitative information on the degree of Cu coverage (Figure 1c). We verified using different negative potentials (Figure S2). The amount of Cu bulk deposition (C2) and dissolution (A1) of Cu is a function of the negative potential limits. The more negative limiting potential showed the larger peaks of bulk Cu deposition (C2) and dissolution peaks (A1). However, the Cu underpotential deposition (C1) and desorption (A2) peaks are well maintained, while the negative limiting potentials change. This indicated that the behavior of Cu bulk deposition (C2) and dissolution (A1) does not affect Cu underpotential deposition (C1) and desorption (A2), suggesting that precise control is capable of forming the f-Cu Pd NC and p-Cu Pd NC catalysts. The Pd nanocube exhibited a single crystal structure with a 0.197 nm lattice spacing parallel to both major facets (Figure 2d). This spacing is consistent with the (200) interplanar spacing corresponding to the face-centered cubic Pd nanocube enclosed by well-extended fcc (100) facets.

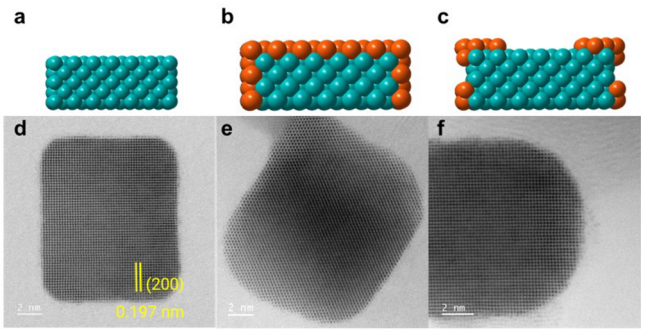

Figure 2. Schematic illustration with complementary bright field (BF)-STEM images of (a, d) Pd NC, (b, e) f-Cu Pd NC, and (c, f) p-Cu Pd NC.

Elemental mapping demonstrated that the f-Cu Pd NC catalyst clearly showed a core−shell structure in which Cu atoms are fully covered on the surface of the Pd nanocube, with Cu accounting for 4.9 at% of the nanoparticle composition (Figure 3). This is additional evidence that the Pd(100) facet is not exposed and only surface-deposited Cu could react with nitrate ions. The p-Cu Pd NC catalyst showed 1.3 at% Cu atoms, which was distributed in a discontinuous coating on the surfaces of Pd nanocubes. We verified 20 wt % metal loading on carbon support for Pd NC/C, f-Cu Pd NC/C, and p-Cu Pd NC/C, confirmed by ICP-MS. The NPs for all catalysts showed a uniform distribution on the carbon support (Figure S3). We measured EDS mapping for all catalysts in low resolution for numerous nanoparticles (Figures S4−S6). In low resolution EDS mapping results, f-Cu Pd NC/C showed 3.9 at % of Cu and p-Cu Pd NC/C exhibited 2.32 at% of Cu. Copper was deposited on Pd and not on the carbon support (Figure S7).

Perchloric acid rather than sulfuric acid was chosen as the supporting electrolyte based on the voltage window. The electrochemical adsorption/desorption and bulk deposition/dissolution of Cu atoms are determined by charge area of peaks during the voltammograms (Figure S21). The surface area of adsorption Cu area estimated from the Cu UPD method is 7.08 m^2 g_{Pd}^{-1} for 0.3−0.8 V_{RHE} (Figure S21a), 24.5 m^2 g_{Pd}^{-1} for 0.25−0.8 V_{RHE} (Figure S21b), 32.7 m^2 g_{Pd}^{-1} for 0.2−0.8 V_{RHE} (Figure S21c), and 36.6 m^2 g_{Pd}^{-1} for 0.1−0.8 V_{RHE} (Figure S21d) assuming 420 C cm^{-2}. This result indicates that the Cu-UPD experiments are well performed and controllable under perchloric acid electrolyte.

Electrocatalytic Performance, Selectivity, and Stability. Electrochemical nitrate reduction (NO_3RR) was carried out in 0.05 M Na_2SO_4 electrolyte with 20 mM NO_3^- (Figure 4a) and electrochemical nitrite reduction (NO_2 RR) was performed in a 0.05 M Na_2SO_4 electrolyte with 2 mM NO_2^- (Figure 4b). We measured the activity of the hydrogen evolution reaction (blank LSV, dashed line) in 0.05 M Na_2SO_4 electrolyte as reference. To compare activity, we collected a partial current density at −0.5 V_{RHE} for NO_3RR and HER, and obtained the current density at −0.25 V_{RHE} for NO_2RR and HER (summarized in Figure S8). Here, we assumed that the

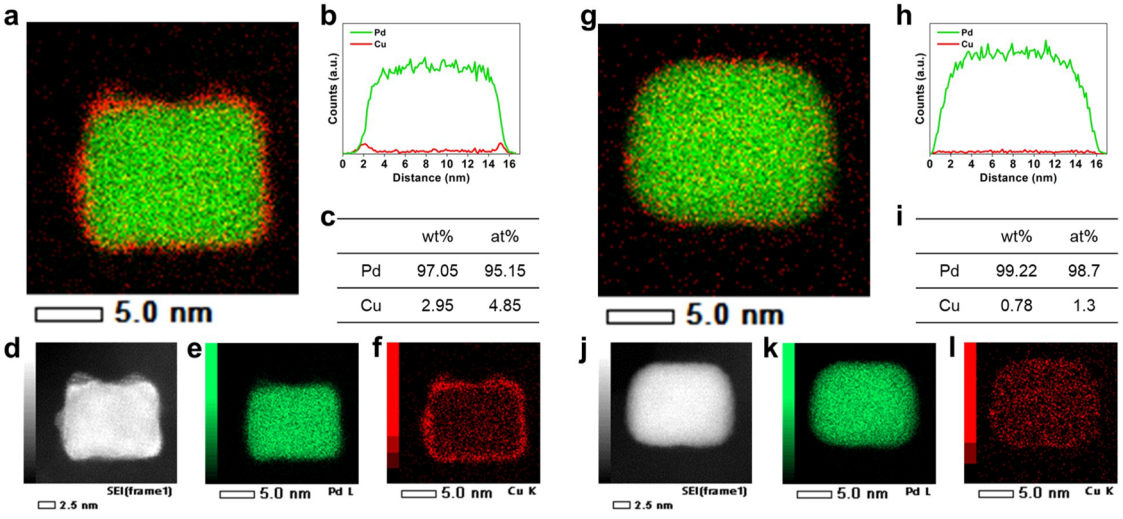

Figure 3. (a, d, e, f) STEM-EDS mapping results, (b) line scanning profiles, and (c) chemical compositions of f-Cu NC. (g, j, k, l) STEM-EDS mapping results, (h) line scanning profiles, and (i) chemical compositions of p-Cu NC.

https://doi.org/10.1021/acscatal.2c04841
ACS Catal. 2023, 13, 87−98

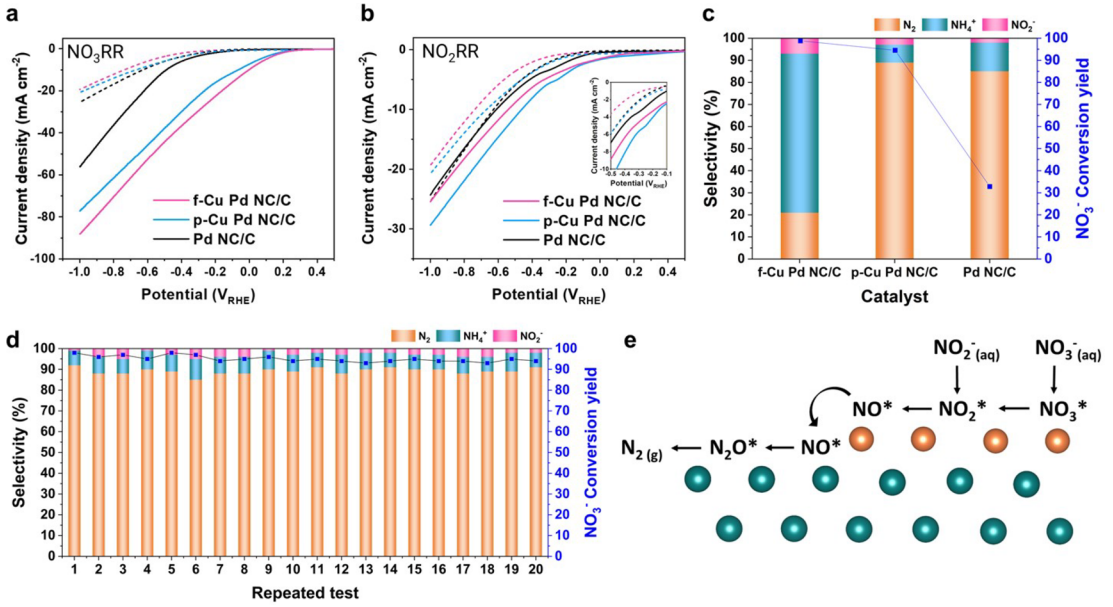

Figure 4. Electrochemical reduction of (a) nitrate and (b) nitrite for Pd NC/C, p-Cu Pd NC/C, and f-Cu Pd NC/C catalysts. Blank LSV curves (dash line) were collected in Ar-purged 0.05 M Na_2SO_4 electrolyte. NO_3RR and NO_2RR tests (solid line) were conducted in Ar-purged 0.05 M Na_2SO_4 + 20 mM NO_3^-, and 0.05 M Na_2SO_4 + 2 mM NO_2^-, respectively. (c) NO_3^- conversion yield and selectivity toward N_2, NO_2^-, and NH_4^+ for Pd NC/C, p-Cu Pd NC/C, and f-Cu Pd NC/C. The NO_3^- conversion yield and selectivity were measured after 4 h electrolysis at −0.5 V_{RHE} in an Ar-purged 0.05 M Na_2SO_4 + 100 ppm of NO_3^-−N electrolyte. (d) Stability of p-Cu Pd NC/C by repeated 20 cycles (80 h electrolysis). (e) Proposed synergistic reaction sequence on the p-Cu Pd NC catalyst, wherein rapid nitrate and nitrite reduction to NO* occurs on Cu domains, NO* migrates to Pd domains, and NO* is reduced selectively to N_2 on the Pd domains.

difference of ECSA values for Pd NC/C, p-Cu Pd NC/C, and f-Cu Pd NC/C are negligible because we build up the small amount of Cu atoms on the same nanoparticle size of Pd NC/C. Pd NC/C exhibited the highest HER activity (5.94 mA cm^{-2}) compared to f-Cu Pd NC/C (3.62 mA cm^{-2}) and p-Cu Pd NC/C (5.85 mA cm^{-2}). The high propensity of Pd to form hydrides through hydrogen adsorption promotes the high HER activity. Despite the high HER activity on Pd, the shape-controlled Pd nanocube, which is exclusively enclosed by only Pd(100) facets, showed good NO_2RR activity. Our previous work demonstrated that $*NO_2$ desorption is 0.19 eV more favorable on the Pd(111) facet compared to the Pd(100) facet.[36] This indicated that NO_2^- will desorb quickly from the surface of Pd(111) before further reduction.

The addition of Cu atoms on the Pd NC, both fully covered Cu Pd NC/C (f-Cu Pd NC/C) and partially covered Cu Pd NC/C (p-Cu Pd NC/C), enhanced the NO_3RR activity of the pure Pd NC/C. The f-Cu Pd NC/C catalyst demonstrated 4.2 times higher NO_3RR activity (44.3 mA cm^{-2} @ −0.5 V_{RHE}) than the Pd NC/C (10.6 mA cm^{-2} @ −0.5 V_{RHE}) (Figure 4a and Figure S8). The f-Cu Pd NC/C catalyst also demonstrated the lowest HER activity (3.62 mA cm^{-2} @ −0.5 V_{RHE}). The low HER activity of the f-Cu Pd NC/C catalyst is due to the fully covered Cu surface, which does not readily form hydrides, and the unique Cu electronic structure. These contribute to increasing nitrate adsorption and electron transfer, constraining HER effectively and catalyzing the NO_3RR processes.[39]

The p-Cu Pd NC/C catalyst also demonstrated a 3.6 times higher activity toward NO_3RR (37.8 mA cm^{-2} @ −0.5 V_{RHE}) than Pd NC/C. The activity; however, remained comparable to that of f-Cu Pd NC/C. This indicates that NO_3RR activity depends on access to Cu sites and that enough active sites are available on either catalyst. This is not surprising given the low concentration of nitrate which was used in the experiments. Both the f-Cu Pd NC/C and the p-Cu Pd NC/C catalysts also have a similar onset potential of 0.25 V_{RHE}, indicating a more positive shift compared to the pure Pd NC control, which has an onset potential of −0.12 V_{RHE}. Even the onset potentials are the same for f-Cu Pd NC/C and p-Cu Pd NC/C catalysts, the partial current density at −0.5 V_{RHE} of p-Cu Pd NC/C (37.8 mA cm^{-2}) is slightly lower than that of f-Cu Pd NC/C (44.3 mA cm^{-2}). This finding indicated that the partially covered Cu coexists with the surface of Pd(100), which is less likely to adsorb nitrate ions compared to Cu. In addition, the surface concentration of Cu atoms is less. Therefore, higher Cu atoms on the surface are more favorable for catalyzing the NO_3RR without considering the exposed Pd surfaces. The deposited Cu atoms could modify the Pd(100) surface structure and have an influence on the adsorbed species during the NO_3RR.

We next examined the NO_2RR activity on the three catalysts. The f-Cu Pd NC/C catalyst demonstrated a slightly higher NO_2RR activity (3.91 mA cm^{-2} @ −0.25 V_{RHE}) than Pd NC/C (2.79 mA cm^{-2} @ −0.25 V_{RHE}). Therefore, in terms of activity toward NO_3RR and NO_2RR, Cu sites in f-Cu Pd NC/C hold more adsorbed NO_2 as a reactant that contributed to achieve higher NO_2RR activity compared to Pd NC/C. The p-Cu Pd NC/C exhibited the best NO_2RR activity (5.00 mA cm^{-2} @ −0.25 V_{RHE}). The p-Cu Pd NC/C also demonstrate an obvious NO_2^- reduction peak around −0.25 V_{RHE} in the enlargement area in Figure 4b. This reduction peak is related to the Pd(100) facet, which showed a similar reduction peak around −0.25 V_{RHE} for Pd NC/C. This indicated that the Pd(100) facets were well exposed on the surface of the f-Cu Pd NC/C catalyst and coexisted with Cu adatoms. This finding indicated that a harmony of Pd and Cu sites is ideal for boosting the reduction processes of nitrate and nitrite.

Next, we quantified the NO_3^- conversion yield for Pd NC/C, p-Cu Pd NC/C, and f-Cu Pd NC/C catalysts that convert

https://doi.org/10.1021/acscatal.2c04841
ACS Catal. 2023, 13, 87−98

the initial total NO_3^- to NO_2^-, NH_4^+, and N_2 as the main products. In Figure 4c, the f-Cu Pd NC/C catalyst demonstrated a high nitrate conversion (98.8%). The p-Cu Pd NC/C showed slightly lower NO_3^- conversion yield (94.5%). The slight decrease in conversion is due to lower concentrations of Cu atoms on the surface. Furthermore, the exposed Pd facets have a lower binding energy of the nitrate compared to that of the Cu, resulting in a slightly lower NO_3^- conversion yield. Pure Pd NC/C showed only 32.8% of the NO_3^- conversion yield. This finding is in agreement with LSV where the magnitude of the current is an indicator of nitrate conversion (Figure 4a).

We also quantified the final product distribution (e.g., N_2, NO_2^-, and NH_4^+) to determine the selectivity of the Pd NC/C, p-Cu Pd NC/C, and f-Cu Pd NC/C catalysts (Figure 4c). The f-Cu Pd NC/C showed excellent NH_4^+ selectivity (72%). This is attributed to Cu as multilayers on the Pd surface. During the electrochemical NO_3RR on the Cu catalyst, the overall reaction rate enhances with occupied d-orbital electrons and unclosed d-orbital shells.[27] In addition, the Cu structure evolves with defects and oxidized status that enable to achieve nearly 100% Faradaic efficiency (FE) and selectivity for NH_4^+ via eight electron transfers.[40,41] The p-Cu Pd NC/C exhibited excellent N_2 selectivity (89%). This is mainly attributed to Cu adatoms that promote the reduction of NO_3^- and NO_2^-, then the existing Pd(100) facets catalyze the reduction of NO to N_2. NO* spillover from the Cu domains to hydrogenated Pd sites plays an important role that contributed to achieve high N_2 selectivity in p-Cu Pd NC/C (Figure 4e). The Pd NC/C exhibited high N_2 selectivity (85%). This slightly lower N_2 selectivity for Pd NC/C catalyst without Cu atoms is attributed to the significantly lower overall conversion of nitrate. Previous work on Pd NC has shown very low NO_3 RR activity in the absence of Cu compared to other Pd shape-controlled nanoparticles with Pd(100) facets.[36]

It should be noted that Pd NC/C and p-Cu Pd NC/C showed only H_2 and N_2 as final gaseous products (Figures S10−12). However, f-Cu Pd NC/C also evolved N_2O gas in addition to N_2 and H_2 (Figure S11). Less detection of H_2 means lower HER activity because fully covered copper multilayers blocked Pd surfaces. One possible reason for the excellent selectivity to N_2 on p-Cu Pd NC/C is that the existence of Cu(100) makes the generation of NO more rapid, which increases the NO* coverage on Pd(100). At higher NO* coverage, N_2O formation is more favorable and Pd(100) sites produced more N_2.

Long-term electrolysis is necessary to achieve practical application. The p-Cu Pd NC/C showed the excellent stability in terms of NO_3^- conversion yield, N_2 selectivity, and structure shape. There was no significant decrease of the NO_3^- conversion yield, maintained over 90%. The long-term electrolysis tests showed the excellent and relatively constant N_2 selectivity even after 20 repeated cycles (80 h electrolysis). The final 20 cycles exhibited 82% of N_2 selectivity. We verified the excellent cyclic and structure stability of p-Cu Pd NC/C after long-term electrochemical NO_3RR electrolysis tests by TEM results (Figures S13 and S14). The majority of p-Cu Pd NC well maintained the nanocube shapes without severe shape collapse and nanoparticle agglomeration after the 20 repeated cycles. After the electrolysis, we measured the leaching concentration of Cu and Pd metals by ICP-MS and detected the negligible amounts for both Pd (3.9 ppb) and Cu (2.2 ppb) in the electrolyte. The p-Cu Pd NC/C exhibited not only highly efficient and N_2 selective electrocatalyst but also highly stable lifetimes for operating test conditions of NO_3RR.

We also examined the long-term stability of the Pd NC/C and f-Cu Pd NC/C electrodes (Figures S13 and S15). Both electrodes did not represent dynamic changes in terms of NO_3^- conversion yield and selectivity. Pd NC/C electrode showed a poor but stable NO_3^- conversion yield (32.8% → 31.2%) and relatively constant selectivity trend (N_2: 85% → 88%, NH_4^+: 13% → 9%, NO_2^-: 2% → 3%). This is because the Pd catalyst is likely to produce N_2 than NH_4^+ from NO_2RR with abounded *H. Due to its low activity for the first nitrate reduction step, the less generated products did not affect the long-term stability.[42] The f-Cu Pd NC/C, which has small amounts of deposited Cu atoms by the UPD approach did not significantly alter a trend of NO_3^- conversion yield (98.8% → 91.1%) and selectivity (N_2: 21% → 26%, NH_4^+: 72% → 70%, NO_2^-: 7% → 4%) during the 20 repeated operations.

MECHANISM

Density Functional Theory (DFT) Calculations. We applied density functional theory (DFT) to investigate the high activity and selectivity toward N_2 achieved by the p-Cu Pd NC catalyst. The results explain the synergistic effect achieved by the simultaneous exposure of Cu and Pd surface domains on the p-Cu Pd NC catalyst, as well as provide insight into the inherent selectivity differences observed for the Cu(100) and Pd(100) surfaces.

As shown in Figure 4c, the selectivity toward NH_4^+, N_2, and NO_2^- on p-Cu Pd NC/C is close to that on Pd NC/C, while the NO_3^- conversion yield on p-Cu Pd NC/C is close to that on f-Cu Pd NC/C. The experimental results strongly indicate that Cu and Pd are playing a synergistic role in NO_3^- reduction on the p-Cu Pd NC catalyst surface, with the NO_3^- reduction activity governed by the Cu domain and the product selectivity determined by the Pd domain. Therefore, we hypothesize that Pd(100) and Cu(100) domains catalyze different steps of the overall nitrate and nitrite reduction pathway. We propose that the rate-determining steps occur on the Cu domain while the selectivity-determining steps occur on the Pd domain, where reaction intermediates spill over from the Cu domain to the Pd domain.

Adsorption is the first step of the electrocatalytic denitrification, and thus we began by computing the adsorption free energy of the key intermediates, i.e., nitrate, nitrite, and NO on both the Cu(100) and Pd(100) surfaces (Figure S16). We found that both nitrate and nitrite bind stronger on the Cu(100) surface than on the Pd(100) surface by 0.33 and 0.18 eV, respectively. This suggests that the initial step of nitrate and nitrite reduction (i.e., adsorption) occurs more readily on the Cu(100) domains. This is consistent with the experimental observation, which shows that the existence of Cu(100) domains enhances NO_3RR and NO_2RR activity. However, after nitrate and nitrite are reduced to NO* on the Cu(100) domain, NO* will tend to migrate to the Pd(100) domain, as the NO* adsorption energy on the Pd(100) surface is significantly more favorable (i.e., NO* adsorption is 0.77 eV more exergonic on the Pd(100) surface than on the Cu(100) surface) (Figure S16). Since Pd NC/C exhibits the highest HER activity in Figure 4a and b, which suggests the possibility of high hydrogen coverage on the Pd domains, we also considered the competitive adsorption of H* and NO* on the Pd surface. We computed the explicit free energy for the migration of NO* from the Cu domain to a hydrogenated site

https://doi.org/10.1021/acscatal.2c04841
ACS Catal. 2023, 13, 87−98

on the Pd domain: $NO^{*-Cu} + H^{*-Pd} \rightarrow \frac{1}{2} H_2 + NO^{*-Pd} + *^{-Cu}$. The free energy of this displacement reaction is thermodynamically favorable (−0.33 eV), which indicates that NO* can displace H* on Pd surfaces. We calculated the NO* migration barrier to confirm the kinetic favorability of NO* migration from the Cu(100) domain to the Pd(100) domain (Figure S17). The migration barrier is surmountable at room temperature on both the Cu(100) and Pd(100) surfaces (i.e., barriers of 0.08 and 0.19 eV on Pd(100) and Cu(100), respectively).

Therefore, after nitrate or nitrite is reduced rapidly on the Cu(100) domains, subsequently generated NO* would migrate to the Pd(100) domain without thermodynamic or kinetic limitations (Figure 4e). Since Cu(100) binds nitrate and nitrite stronger and is known to quickly convert nitrate to nitrite,[19,22,24,40,43,44] and Pd(100) is selective to N_2,[45] a synergistic effect in the bimetallic system, wherein there is NO* spillover from Cu to Pd, potentially explains the excellent performance of the p-Cu Pd NC catalyst in achieving selective nitrate reduction to N_2.[22−24]

The experimental observations in Figure 4c suggest that Cu(100) is selective to NH_4^+ formation and Pd(100) is selective to N_2 production. NO* is a known selectivity-determining intermediate in the electrochemical denitrification reaction.[46,47] Thus, to explain for the selectivity difference between Cu and Pd, we investigated the reaction pathway after NO* forms on the Pd(100) and Cu(100) surfaces. The direct NO* dissociation barrier has been previously calculated on various metal surfaces (i.e., Rh, Cu, Pd, Pt)[46,48−50] and was found to be prohibitively high at room temperature. Chun et al.[46] investigated the (NO−NO)* dimer formation on the Cu(211) surface and found dimer formation to be less favorable than H-insertion in the NO* molecule. On the Pd(100) surface, we found that the (NO−NO)* dimer is not stable, as the N−N bond broke spontaneously during all our attempts at structural optimization. Therefore, in this work, we focused on the NO* hydrogenation pathway. We compared the favorability of HNO* and NOH* formation on the Pd(100) and Cu(100) surfaces, where HNO* is formed by hydrogenation of the nitrogen atom in NO* and NOH* is formed by hydrogenation of the oxygen atom. In both cases, we considered both direct H-insertion and H-insertion via a water-assisted proton shuttle.[51,52] We found that the proton-shuttle yields a lower barrier for NOH* formation compared to direct hydrogenation. However, the proton-shuttle did not significantly alter the barrier for the formation of HNO*, as the geometry of the water shuttle incurs significant strain because H* already lies close to the nitrogen atom of the surface-bound NO*. On the Pd(100) surface, the reaction energy and activation barrier to form HNO* with the proton-shuttle (0.37 and 0.80 eV, respectively, Figure S18) are close to those for direct hydrogenation (0.33 and 0.88 eV, respectively, Figure 5a).

Comparisons of the reaction energy and activation barrier for H* + NO* → HNO* and H* + NO* → NOH* on Pd(100) and Cu(100) yield insights into the selectivity differences of the two metals (Figure 5a, b). On the Pd(100) surface, when the oxygen atom in NO* is targeted for hydrogenation (i.e., NOH* formation), the reaction barrier and the reaction energy are 0.48 and 0.21 eV lower, respectively, than those when the nitrogen atom is targeted (i.e., HNO* formation). This suggests that the Pd(100) surface is more selective to NOH* formation both kinetically and thermodynamically. However, on the Cu(100) surface, HNO* formation is kinetically and thermodynamically more favorable than NOH* formation by 0.18 and 0.28 eV, respectively. Therefore, the Cu(100) surface is more selective to HNO* formation. The different selectivity toward HNO* or NOH* on the Cu and Pd surfaces likely leads to different final products (i.e., NH_4^+ or N_2), where it is expected that

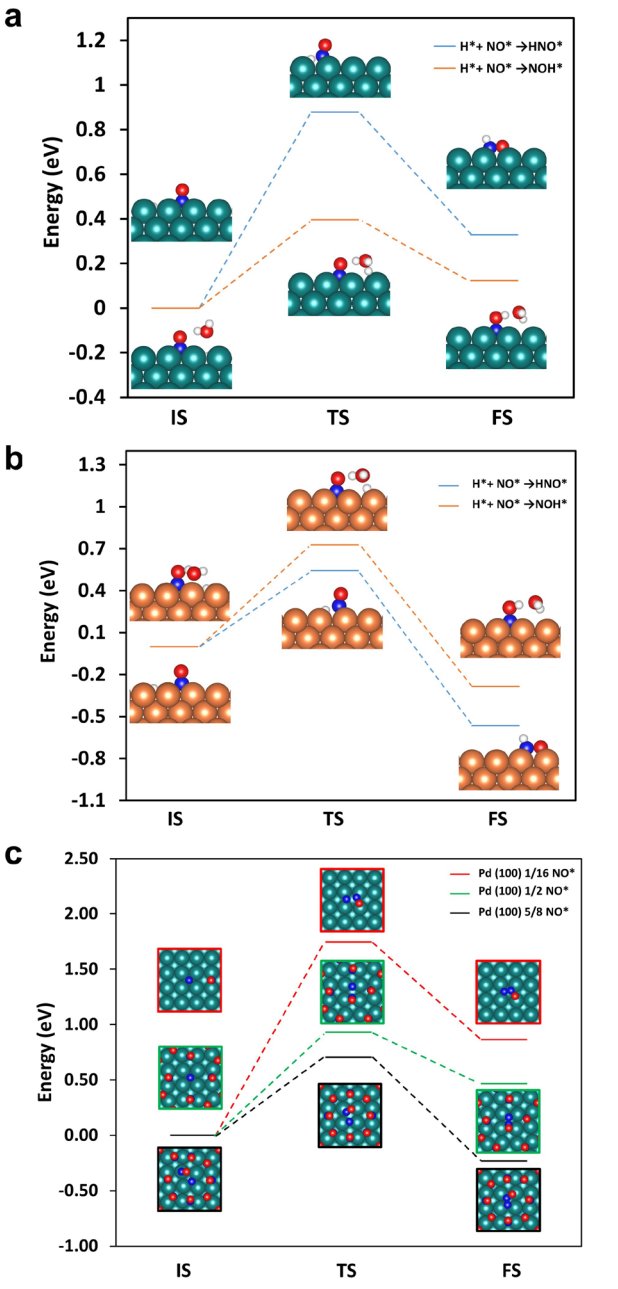

Figure 5. Reaction energy diagram of H* + NO* → HNO* (blue line) and H* + NO* → NOH* (orange line) on (a) Pd(100) and (b) Cu(100) surfaces at 1/16 NO* coverage. (c) Reaction energy diagram of N* + NO* → N_2O* at 1/16 NO* coverage (red line), 1/2 NO* coverage (green line), and 5/8 NO* coverage (black line) on Pd(100). The insets show the structure of the initial state (IS), transition state (TS), and final state (FS) of the reaction process. The white, red, blue, green, and orange spheres represent H, O, N, Pd, and Cu, respectively.

https://doi.org/10.1021/acscatal.2c04841
ACS Catal. 2023, 13, 87−98

hydrogenation of the nitrogen site in NO* will lead to the more hydrogenated product (i.e., HNO* yields NH_4^+).

In addition to the nonelectrochemical reaction pathway for NOH* and HNO* formation, which starts with surface-adsorbed H* and NO*, we also considered NOH* and HNO* formation in an electrochemical framework. Here, the initial state consists of adsorbed NO* on the catalyst surface, a proton in the electrolyte, and an electron in the electrode surface.[53] We compared the reaction diagram of the reactions: $H^+ + e^- + NO^* \rightarrow HNO^*$ and $H^+ + e^- + NO^* \rightarrow NOH^*$ on Pd(100) and Cu(100) surface at 0 V_{RHE}, which leads to the same conclusion regarding selectivity toward NOH* on Pd and toward HNO* on Cu (Figure S19). On the Pd(100) surface, although HNO* formation is slightly more thermodynamically favorable than NOH* formation by 0.01 eV, the activation barrier of HNO* formation is much higher than NOH* formation by 0.48 eV. On the Cu(100) surface, the reaction barrier and the reaction energy for HNO* formation are 0.28 and 0.20 eV lower than those of NOH* formation, respectively. This further confirms the selectivity to HNO* on the Cu(100) surface.

On the Pd(100) surface, after NOH* is formed, NOH* can readily dissociate with the assistance of a water-mediated proton shuttle to form N* (i.e., $NOH^* + H^* \rightarrow N^* + H_2O + *$) which has a highly negative reaction energy (−1.38 eV) and a surmountable barrier at room temperature (0.47 eV) (Figure S20). N* can couple with NO* to generate N_2O, which is a precursor of N_2.[54] We found N−NO* coupling becomes more favorable both thermodynamically and kinetically at higher NO* coverage on the Pd(100) surface, as the kinetic barrier decreases from 1.75 eV at an NO* coverage of 1/16 to 0.70 eV at an NO* coverage of 5/8. Thus, Pd(100) becomes more selective to N_2 at higher NO* coverage, which is consistent with experimental results[54] and with our NO* Cu-to-Pd spillover hypothesis (Figure 5c). HNO* forms on the Cu(100) surface, which makes a stable N−H bond at the onset that will favor NH_4^+ formation, as well as prevents N* formation and in turn N−NO* coupling on the pathway toward N_2.

EXPERIMENTAL METHODS

Materials and Methods. *Materials.* Palladium(II) sodium chloride (Na_2PdCl_4, 98%), copper(II) chloride dihydrate ($CuCl_2{\cdot}2H_2O$, ≥99.0%), polyvinylpyrrolidone (PVP, M.W. 55000), L-ascorbic acid ($C_6H_8O_6$, 99%), potassium bromide (KBr, ≥99%), sodium sulfate (Na_2SO_4, ≥99%), sodium nitrate ($NaNO_3$, ≥99%), sodium nitrite ($NaNO_2$, ≥99%), sulfanilamide ($C_6H_8N_2O_2S$, ≥98%), *N*-(1-naphthyl) ethylenediamine dihydrochloride ($C_{12}H_{14}N_2$, ≥98%), perchloric acid ($HClO_4$, 70%), phosphoric acid (H_3PO_4, ≥85%), sodium nitroferricyanide(III) dihydrate ($C_5FeN_6Na_2O{\cdot}2H_2O$, ≥99%), sodium hydroxide (NaOH, ≥ 97%), sodium hypochlorite solution (NaClO, ≥98%), salicylic acid ($C_7H_6O_3$, ≥99%), sodium citrate dihydrate ($C_6H_5Na_3O_7{\cdot}2H_2O$, ≥99%) were all purchased from Sigma-Aldrich. Vulcan XC-72R carbon powder used as a support obtained from the Cabot Corporation. The Nafion membrane was purchased from Fuel Cell Store Company and TNTplus vial test kit for nitrate measurement was purchased from HACH company. Ultrapure water (18.2 MΩ) was used from Millipore Milli-Q.

Pd Nanocube Synthesis. We used a previously reported protocol with minor modification,[55−57] which was also used in our previous work.[36] Na_2PdCl_4 (8 mg), L-ascorbic acid (AA, 60 mg), KBr (400 mg), and PVP (105 mg) were used as a Pd precursor, reducing agent, capping agent, and surfactant, respectively. First, AA, KBr, and PVP were dissolved in ultrapure water (8 mL) at 85 °C for 15 min. Then, the aqueous Na_2PdCl_4 solution (3 mL) was added and kept at 85 °C for 3 h. The suspension was cooled to room temperature. Pd nanocube nanoparticles were washed with ultrapure water and ethanol several times and collected by centrifugation.

Deposition of Pd Nanocubes Nanoparticles on Carbon Support. For electrochemical characterizations, we used Vulcan carbon XC72R as a support to deposit Pd nanocube nanoparticles by using 3 h of ultrasonication in ethanol. We set the Pd metal loading for 20 wt % confirmed by ICP-MS result.

Preparation of f-Cu Pd NC/C and p-Cu Pd NC/C Catalysts. We conducted the underpotential deposition of Cu on the Pd NC/C catalyst at glassy carbon electrode (GCE) or carbon paper electrode. After the electrochemical conditioning step for surface cleaning in 0.1 M $HClO_4$ electrolyte, we controlled the deposition amounts of Cu on Pd NC/C catalysts by selecting different stopping potentials between 0.3 and 0.8 V_{RHE} in the presence of copper salt (e.g., 3 mM $CuCl_2$) (Figure S1).

Catalyst Characterizations. TEM and HRTEM images (FEI Tecnai F20) were acquired at 200 kV operation. Aberration corrected high-angle annular dark field scanning TEM (HAADF-STEM) images and complementary energy dispersive X-ray spectrum (EDS) images were obtained on JEOL JEM2200FS (200 kV) equipped with a third-order CEOS aberration corrector and a Bruker XFlash silicon drift detector. The TEM samples were dispersed by ultrasonication in ethanol and dropped on gold grid (Electron Microscopy Science Co.), and then dried for analysis. Inductively coupled plasma mass spectrometer (ICP-MS, PerkinElmer Elan DRC) was used to determine the 20 wt % concentrations of Pd nanocube for the deposition at carbon support and measure the leaching concentrations of Pd and Cu after electrolysis tests.

Electrochemical NO_3RR and NO_2RR Tests. A standard three-electrode electrochemical cell (Pine Research) connected with potentiostat was used. Working electrode is prepared by drop casting of catalyst ink on glassy carbon electrode at ring disk electrode (RDE). Pd NC/C catalyst was dissolved into a mixture of Nafion ionomer solution (5 wt %, 20 μL mL^{-1}), ultrapurewater and isopropanol acolohol (1.5 mg mL^{-1}). The Pd metal loading on the GCEs was 15 μg_{Pd} cm^{-2}, and it was dried under ambient conditions in air. A Pt wire and Ag/AgCl (saturated potassium chloride) were used as a counter electrode and reference electrode, respectively. We used hydrogen gas purging into electrolyte and Pt electrode to convert a reversible hydrogen electrode (RHE) from measured potentials. The surface of Pd NC/C electrocatalyst was electrochemically cleaned by sweeping potentials (−0.4 to 0.8 V_{RHE}) for 200 cycles in 0.05 M Na_2SO_4 electrolyte before measuring the LSV curve. Then, we introduced Cu and measured the LSV curves for p-Cu Pd NC/C and f-Cu Pd NC/C electrocatalysts. The LSV data of NO_3RR and NO_2RR were measured while rotating at 1000 rpm with a scan rate of 50 mV s^{-1}. The potential sweeps started at 0.5 V_{RHE} to −1.0 V_{RHE} for electrochemical NO_3RR and NO_2RR. An Ar purged environment in all electrolytes was supported to remove possible remained oxygen in electrolyte. We added 20 mM NO_3 or 2 mM NO_2 into 0.05 M Na_2SO_4 electrolyte for NO_3RR and NO_2RR activity, respectively. Electrolysis tests were performed in a two-chamber electrolytic cell connected with the potentiostat and in situ mass spectrometry for

https://doi.org/10.1021/acscatal.2c04841
ACS Catal. 2023, 13, 87−98

measuring gaseous products. The working electrode geometric area was controlled with 0.25 cm^2. We prepared pristine Pd NC/C catalyst ink first and spray-coated on carbon paper as a working electrode. To fabricate bulk scale of f-Cu PdNC/C and p-Cu PdNC/C electrodes, we conducted Cu UPD method with a pristine Pd NC/C coated on carbon paper and deposited Cu atoms as same conditions with half-cell tests. By controlling the sweeping potential Ag/AgCl reference electrode was placed in the cathode chamber and Pt wire was used as a counter electrode and placed in the anode chamber. The electrolytes in the cathode and anode chambers both were 0.05 M Na_2SO_4 electrolyte. The 100 ppm of NO_3^-−N was only added into the cathode compartment. Chronoamperometry (CA) was performed at −0.5 V_{RHE} for 4 h. Long-term electrolysis for the stability of p-Cu Pd NC/C electrode was performed at −0.5 V_{RHE} electrolysis for 4 h and repeated 20 cycles (80 h electrolysis).

Determinations of Products. Ion concentrations of NO_3^-−N, NO_2^-−N and NH_4^+−N are analyzed by a titration technique using the ultraviolet−visible (UV−vis) spectrophotometer based on our previous study.[36] NO_3^-−N concentrations were estimated from a calibration curve obtained from the absorption intensities and wavelength (345 nm) by using the nitrate kit (HACH Co.). The detection of limit for NO_3^-−N is 0.4 ppm. NO_2^-−N ion concentrations were determined from a calibration curve obtained from the absorption intensities at a wavelength (540 nm) by using a color reagent. The color reagent is prepared by dissolving *N*-(1-naphthyl) ethylenediamine dihydrochloride (0.2 g) and *p*-aminobenzenesulfonamide (4 g) into phosphoric acid (10 mL) and ultrapure water (50 mL) solutions. The detection of limit for NO_2^-−N is 0.02 ppm. NH_4^+−N was estimated using the indophenol blue method. We prepared 5 wt % salicylic acid in 1 M NaOH solution and 5 wt % sodium citrate that was added into samples. Then, 0.05 M NaClO (1 mL) and 1 wt % $C_5FeN_6Na_2O$ solution (0.1 mL) were added into 1 mL of samples. The change from colorless to blue color was detected in the absorbance at a wavelength (655 nm). The detection of limit for NH_4^+−N is 0.2 ppm. For gaseous products measurement, an in situ mass spectrometer (Cirrus 2, MKS Instruments) was attached to the sealed two chamber cell. We used the ultrahigh purity Air carrier gas for the calibration. The typical atmospheric pressure entry of 760 Torr is used, the entered mass was 28 for diatomic nitrogen, and the percentage for the contribution of mass 28 was 78%. The multiplier mass was set to 29 for a 0.57% contribution to the partial pressure of air. Ultrahigh purity Ar carrier gas was purged into the cathode chamber at a 20 mL min^{-1} during the electrolysis. All electrolysis tests were only initiated after the gas analyzer signal was stabilized.

Calculation of NO_3^- Conversion Rate and N_2 Selectivity.

$$NO_3^- \text{ conversion rate} = \frac{\Delta C(NO_3^-)}{C_0(NO_3^-\text{—N})} \times 100\% \quad (1)$$

$$S(NO_2^-)\% = \frac{C_t(NO_2^-\text{—N})}{\Delta C(NO_3^-\text{—N})} \times 100\% \quad (2)$$

$$S(NH_4^+)\% = \frac{C_t(NH_4^+\text{—N})}{\Delta C(NO_3^-\text{—N})} \times 100\% \quad (3)$$

$$S(N_2)\% = \frac{\Delta C(NO_3^-\text{—}N) - C_t(NO_2^-\text{—N}) - C_t(NH_4^+\text{—N})}{\Delta C(NO_3^-\text{—N})} \times 100\% \quad (4)$$

$\Delta C_0(NO_3^-\text{—N})$ is the difference of NO_3^- ion concentration between initial and after electrolysis tests and C_0 is the initial NO_3^- ion concentration. The electrolyte volume in the cathode compartment is 20 mL of 0.05 M Na_2SO_4 including 100 ppm of NO_3^-−N. The C_t is concentration change after the reduction time, and selectivity of N_2 is calculated by total nitrogen mass balance considering NO_3^-−N, NO_2^-−N, and NH_4^+−N.

Theoretical Calculation Method. We applied the Vienna ab initio Simulation Package (VASP) version 5.4.4[58,59] for the density functional theory (DFT) calculations. The nuclei and frozen core electrons were treated using the projector augmented wave (PAW)[60] formalism with VASP default potentials.[61] The valence electrons (N-$2s^22p^3$, O-$2s^22p^4$, H-$1s^1$, Cu-$3d^{10}4s^1$, and Pd-$4d^95s^1$) were treated self-consistently. The Perdew−Burke−Ernzerhof (PBE) generalized gradient approximation (GGA) exchange-correlation functional[62] was employed. The van der Waals interactions were described by Grimme's D3 dispersion.[63] All calculations were spin-polarized with a 400 eV kinetic energy cutoff for the plane-wave basis sets. The calculations were performed on four layers of Cu(100) and Pd(100) surfaces with the bottom layer of the slab fixed in bulk positions. The periodic slabs were separated by at least 15 Å in the *z* direction. A Monkhorst−Pack (MP)[64] k-point mesh of 4 × 4 × 1 was sampled on 4 × 4 periodic supercells for both Cu(100) and Pd(100) slabs. The electronic energy was converged to within 10^{-5} eV for each electronic self-consistent-field cycle and forces in reported geometries were converged to within 20 meV $Å^{-1}$. The Methfessel−Paxton smearing was set at σ = 0.2 eV.[65] A dipole correction perpendicular to the surface was applied for all calculations. Transition states (TS) were found using the climbing image nudged elastic band (CI-NEB) method[66,67] with the force converged to within 50 meV $Å^{-1}$, where the dimer method[68] was applied to refine the search for saddle points. The TS structures were confirmed to have only one imaginary frequency.

The absolute free energies of species (G^0_{298K}) were calculated using eq 5 derived from standard formulas from statistical mechanics:[69]

$$G^0_{298K} = E_{SCF} + ZPE + H_{298K} - TS_{298K} \quad (5)$$

where E_{SCF} represents the ground state electronic energy at 0 K, ZPE represents the zero-point energy, T represents the temperature (298 K), H_{298K} is the enthalpy correction at 298 K, and S_{298K} represents the entropy at 298 K.[70] Translational and rotational degrees of freedom were neglected for species chemisorbed on the surface. Vibrational contributions of the surface species were calculated from frequencies computed with a finite difference analysis in VASP, where the surface metal atoms were fixed. The E_{SCF} energies of HNO_3, HNO_2, NO, and H_2 were computed separately in a 20 × 20 × 20 $Å^3$ unit cell with 1 × 1 × 1 MP *k*-points sampling in VASP. The ZPE + H_{298K} − TS_{298K} correction values for the molecules were directly calculated using the NorthWest Chemistry (NWChem) modeling software[71] for the equivalent molecule geometry.

To calculate the adsorption free energy of the reaction shown in eqs 6−8

https://doi.org/10.1021/acscatal.2c04841
ACS Catal. 2023, 13, 87−98

$$NO_3^- + * \rightarrow NO_3^* + e^- \quad (6)$$

$$NO_2^- + * \rightarrow NO_2^* + e^- \quad (7)$$

$$NO + * \rightarrow NO^* \quad (8)$$

where the * represents Cu(100) and Pd(100) surface sites, we used the same calculation method described in our previous work[36] (eqs 9–11):

$$\Delta G_{ads}(NO_3^-) = G_{NO_3^*} + [G_{e^-} + G_{H^+}] - [G_{NO_3^-} + G_{H^+}] - G_* = G_{NO_3^*} - G_* + \left[\frac{1}{2}G_{H_2} - eU_{RHE}\right] - [G_{HNO_3} + 2.303RT(pK_a - pH)] \quad (9)$$

$$\Delta G_{ads}(NO_2^-) = G_{NO_2^*} + [G_{e^-} + G_{H^+}] - [G_{NO_2^-} + G_{H^+}] - G_* = G_{NO_2^*} - G_* + \left[\frac{1}{2}G_{H_2} - eU_{RHE}\right] - [G_{HNO_2} + 2.303RT(pK_a - pH)] \quad (10)$$

$$\Delta G_{ads,NO} = G_{NO^*} - G_* - G_{NO} \quad (11)$$

where $G_{NO_3^*}$, $G_{NO_2^*}$, and G_{NO^*} are the free energy of NO_3, NO_2, and NO adsorbed on the metal surfaces, separately, G_{e^-} is the free energy of the electron, G_{H^+} is the free energy of the proton. The free energy of the electron–proton pair was computed using the computational hydrogen electrode model.[72] G_* is the energy of the Cu(100) or Pd(100) surface. G_{H_2} is the free energy of the H_2 at 1 atm. U_{RHE} is the applied potential referenced to the reversible hydrogen electrode (RHE), R is the gas constant, T is the temperature, and $G_{NO_3^-}$ is the free energy of NO_3^- at a concentration of 20 mM, $G_{NO_2^-}$ is the free energy of NO_2^- at a concentration of 2 mM. $G_{NO_3^-}$ and $G_{NO_2^-}$ were computed using a thermodynamic cycle to avoid calculating the energy of an anion in the periodic simulation cell, where the free energy of the anion is computed from the free energy of its neutral acid and associated pK_a. G_{HNO_3} is the free energy of HNO_3 at a HNO_3 concentration of 20 mM, and the pK_a of HNO_3 is −1.4.[73,74] G_{HNO_2} is the free energy of HNO_2 at a HNO_2 concentration of 2 mM, and the pK_a of HNO_2 is 3.25.[75] G_{NO} is the free energy of NO at a concentration of 0.2 mM. The adsorption free energy was calculated at pH = 7, 298 K, and a potential of −0.5 V_{RHE}.

The NO* migration from Cu to the hydrogenated Pd site is described by eq 12:

$$NO^{*-Cu} + H^{*-Pd} \rightarrow \frac{1}{2}H_2 + NO^{*-Pd} + *^{-Cu} \quad (12)$$

where $*^{-Cu}$ and $*^{-Pd}$ represent Cu and Pd sites, respectively. The free energy of this migration step is computed with eq 13:

$$\Delta G = G_{*-Cu} + G_{NO*-Pd} + \frac{1}{2}G_{H_2} - G_{H*-Pd} - G_{NO*-Cu} \quad (13)$$

where G_{NO*-Pd} and G_{*-Cu} are the free energies of the Cu(100) surface with and without NO* adsorbed, respectively. G_{H_2} is the free energy of the H_2 (g) at 1 atm. G_{NO*-Pd} and G_{NO*-Cu} are the free energy of NO* and H* adsorbed on the Pd(100) surface, respectively.

The potential-dependent activation barriers for the reaction

$$A^* + H^+ + e^- \rightarrow AH^*$$

at a potential of U_{RHE} were calculated using eq 11 based on the methodology of Janik and co-workers:[53]

$$E_a(U_{RHE}) = E_a(U_0) + \beta F[U - U_0] \quad (14)$$

$$U_0 = -\frac{G_{A^*+H^*} - G_{A^*+*} - \frac{1}{2}G_{H_2(g)}}{e} \quad (15)$$

$E_a(U_0)$ is the activation barrier at the equilibrium potential for the adsorption of a proton–electron pair on the metal surface. β represents the symmetry factor, which is assumed to be 0.5 in all steps, F is the Faraday constant, and e is the positive elementary charge. $G_{H^*+A^*}$ denotes the free energy when both H* and reactant A* are adsorbed on the metal surface. G_{A^*+*} represents the energy when only reactant A^* is adsorbed on the metal surface so there is an open adjacent site denoted as *. $G_{H_2(g)}$ is the free energy of H_2 at 1 atm. Geometries of converged structures are provided at https://github.com/tsenftle/PdCu_Selectivity.

■ ASSOCIATED CONTENT

Supporting Information

The Supporting Information is available free of charge at https://pubs.acs.org/doi/10.1021/acscatal.2c04841.

Cyclic voltammogram for copper under potential deposition, TEM and EDS mapping of nanocrsytals, in situ mass spectrometry product analyses, adsorption configuration graphics from DFT, table of relevant performance from literature, and additional experimental details, materials, and methods (PDF)

■ AUTHOR INFORMATION

Corresponding Authors

Seung Woo Lee − *George W. Woodruff School of Mechanical Engineering, Georgia Institute of Technology, Atlanta, Georgia 30313, United States;* orcid.org/0000-0002-2695-7105; Email: seung.lee@me.gatech.edu

Thomas P. Senftle − *Department of Chemical and Biomolecular Engineering, Rice University, Houston, Texas 77005, United States;* orcid.org/0000-0002-5889-5009; Email: tsenftle@rice.edu

Marta C. Hatzell − *George W. Woodruff School of Mechanical Engineering and Department of Chemical and Biomolecular Engineering, Georgia Institute of Technology, Atlanta, Georgia 30313, United States;* orcid.org/0000-0002-5144-4969; Email: marta.hatzell@me.gatech.edu

Authors

Jeonghoon Lim − *George W. Woodruff School of Mechanical Engineering, Georgia Institute of Technology, Atlanta, Georgia 30313, United States;* Present Address: Lawrence Berkeley National Laboratory, Berkeley, California 94720, United States

Yu Chen − *Department of Chemical and Biomolecular Engineering, Rice University, Houston, Texas 77005, United States*

https://doi.org/10.1021/acscatal.2c04841
ACS Catal. 2023, 13, 87−98

David A. Cullen − *Center for Nanophase Materials Sciences, Oak Ridge National Laboratory, Oak Ridge, Tennessee 37831, United States;* orcid.org/0000-0002-2593-7866

Complete contact information is available at: https://pubs.acs.org/10.1021/acscatal.2c04841

Notes

The authors declare no competing financial interest.

■ ACKNOWLEDGMENTS

This material is based upon work supported by the National Science Foundation under Grant No. 1846611 and 1933646. M.C.H. and J.L. were supported by the National Science Foundation through the Center for Advancing Sustainable and Distributed Fertilizer Production (CASFER) under Grant No. EEC-2133576. Y.C. and T.P.S. were supported by the National Science Foundation through the Nanosystems Engineering Research Center for Nanotechnology-Enabled Water Treatment (NEWT) under Grant No. EEC-1449500. This material was supported by the Gordon and Betty Moore Foundation—Moore Inventor Fellowship (Grant number #10615). Electron microscopy research was supported by the Center for Nanophase Materials Sciences (CNMS), which is a US Department of Energy, Office of Science User Facility at Oak Ridge National Laboratory.

■ REFERENCES

(1) Rupert, M. G. Decadal-scale changes of nitrate in ground water of the United States, 1988−2004. *Journal of Environmental Quality* **2008**, *37*, S-240.

(2) Burow, K. R.; Nolan, B. T.; Rupert, M. G.; Dubrovsky, N. M. Nitrate in groundwater of the United States, 1991- 2003. *Environ. Sci. Technol.* **2010**, *44*, 4988−4997.

(3) Martínez, J.; Ortiz, A.; Ortiz, I. State-of-the-art and perspectives of the catalytic and electrocatalytic reduction of aqueous nitrates. *Appl. Catal. B: Environmental* **2017**, *207*, 42−59.

(4) U.S. EPA. *Ground Water and Drinking Water Table of Regulated Drinking Water Contaminants*; 2017.

(5) Wu, D.; Li, X.; Li, X. Toward Energy Neutrality in Municipal Wastewater Treatment: A Systematic Analysis of Energy Flow Balance for Different Scenarios. *ACS ES&T Water* **2021**, *1*, 796−807.

(6) Burge, S.; Halden, R.*Nitrate and Perchlorate Removal from Groundwater by Ion Exchange*; 1999.

(7) Lee, C.-S.; Guo, S.; Rho, H.; Levi, J.; Garcia-Segura, S.; Wong, M. S.; Gardea-Torresdey, J.; Westerhoff, P. Unified Metallic Catalyst Aging Strategy and Implications for Water Treatment. *Environ. Sci. Technol.* **2021**, *55*, 11284−11293.

(8) Heck, K. N.; Garcia-Segura, S.; Westerhoff, P.; Wong, M. S. Catalytic converters for water treatment. *Accounts of chemical research* **2019**, *52*, 906−915.

(9) Anglada, A.; Urtiaga, A.; Ortiz, I. Contributions of electrochemical oxidation to waste-water treatment: fundamentals and review of applications. *J. Chem. Technol. Biotechnol.* **2009**, *84*, 1747−1755.

(10) Birdja, Y.; Yang, J.; Koper, M. Electrocatalytic reduction of nitrate on tin-modified palladium electrodes. *Electrochim. Acta* **2014**, *140*, 518−524.

(11) Beltrame, T. F.; Zoppas, F. M.; Gomes, M. C.; Ferreira, J. Z.; Marchesini, F. A.; Bernardes, A. M. Electrochemical nitrate reduction of brines: Improving selectivity to N2 by the use of Pd/activated carbon fiber catalyst. *Chemosphere* **2021**, *279*, 130832.

(12) Favarini Beltrame, T.; Gomes, M. C.; Marder, L.; Marchesini, F. A.; Ulla, M. A.; Moura Bernardes, A. Use of copper plate electrode and Pd catalyst to the nitrate reduction in an electrochemical dual-chamber cell. *Journal of Water Process Engineering* **2020**, *35*, 101189.

(13) Duca, M.; Cucarella, M. O.; Rodriguez, P.; Koper, M. T. Direct reduction of nitrite to N2 on a Pt (100) electrode in alkaline media. *J. Am. Chem. Soc.* **2010**, *132*, 18042−18044.

(14) Duca, M.; Figueiredo, M. C.; Climent, V.; Rodriguez, P.; Feliu, J. M.; Koper, M. T. Selective catalytic reduction at quasi-perfect Pt (100) domains: a universal low-temperature pathway from nitrite to N2. *J. Am. Chem. Soc.* **2011**, *133*, 10928−10939.

(15) Dima, G.; Beltramo, G.; Koper, M. Nitrate reduction on single-crystal platinum electrodes. *Electrochimica acta* **2005**, *50*, 4318−4326.

(16) Chen, T.; Li, H.; Ma, H.; Koper, M. T. Surface modification of Pt (100) for electrocatalytic nitrate reduction to dinitrogen in alkaline solution. *Langmuir* **2015**, *31*, 3277−3281.

(17) Pizarro, A.; Molina, C.; Rodriguez, J.; Epron, F. Catalytic reduction of nitrate and nitrite with mono-and bimetallic catalysts supported on pillared clays. *Journal of Environmental Chemical Engineering* **2015**, *3*, 2777−2785.

(18) Calvo, L.; Gilarranz, M. A.; Casas, J. A.; Mohedano, A. F.; Rodriguez, J. J. Denitrification of water with activated carbon-supported metallic catalysts. *Industrial & engineering chemistry research* **2010**, *49*, 5603−5609.

(19) Garcia-Segura, S.; Lanzarini-Lopes, M.; Hristovski, K.; Westerhoff, P. Electrocatalytic reduction of nitrate: Fundamentals to full-scale water treatment applications. *Appl. Catal. B: Environmental* **2018**, *236*, 546−568.

(20) Su, J. F.; Kuan, W.-F.; Chen, C.-L.; Huang, C.-P. Enhancing electrochemical nitrate reduction toward dinitrogen selectivity on Sn-Pd bimetallic electrodes by surface structure design. *Appl. Catal. A: General* **2020**, *606*, 117809.

(21) Soto-Hernández, J.; Santiago-Ramirez, C.; Ramirez-Meneses, E.; Luna-Trujillo, M.; Wang, J.-A.; Lartundo-Rojas, L.; Manzo-Robledo, A. Electrochemical reduction of NOx species at the interface of nanostructured Pd and PdCu catalysts in alkaline conditions. *Appl. Catal. B: Environmental* **2019**, *259*, 118048.

(22) Chen, Z.; Wang, Y.; Wang, J.; Hu, Z.; Teng, W.; Fan, J.; Zhang, W. Enhanced activity and selectivity of electrocatalytic denitrification by highly dispersed CuPd bimetals on reduced graphene oxide. *Chem. Eng. J.* **2021**, *416*, 129074.

(23) Wang, J.; Teng, W.; Ling, L.; Fan, J.; Zhang, W.-x.; Deng, Z. Nanodenitrification with bimetallic nanoparticles confined in N-doped mesoporous carbon. *Environmental Science: Nano* **2020**, *7*, 1496−1506.

(24) De Vooys, A.; Van Santen, R.; Van Veen, J. Electrocatalytic reduction of NO3- on palladium/copper electrodes. *J. Mol. Catal. A: Chem.* **2000**, *154*, 203−215.

(25) Ghodbane, O.; Roué, L.; Bélanger, D. Study of the electroless deposition of Pd on Cu-modified graphite electrodes by metal exchange reaction. *Chem. Mater.* **2008**, *20*, 3495−3504.

(26) Fan, J.; Xu, H.; Lv, M.; Wang, J.; Teng, W.; Ran, X.; Gou, X.; Wang, X.; Sun, Y.; Yang, J. Mesoporous carbon confined palladium−copper alloy composites for high performance nitrogen selective nitrate reduction electrocatalysis. *New J. Chem.* **2017**, *41*, 2349−2357.

(27) Zeng, Y.; Priest, C.; Wang, G.; Wu, G. Restoring the nitrogen cycle by electrochemical reduction of nitrate: progress and prospects. *Small Methods* **2020**, *4*, 2000672.

(28) Duca, M.; Sacré, N.; Wang, A.; Garbarino, S.; Guay, D. Enhanced electrocatalytic nitrate reduction by preferentially-oriented (100) PtRh and PtIr alloys: the hidden treasures of the 'miscibility gap'. *Appl. Catal. B: Environmental* **2018**, *221*, 86−96.

(29) Taguchi, S.; Feliu, J. M. Electrochemical reduction of nitrate on Pt (S)[n (1 1 1)×(1 1 1)] electrodes in perchloric acid solution. *Electrochimica acta* **2007**, *52*, 6023−6033.

(30) Yang, J.; Duca, M.; Schouten, K. J. P.; Koper, M. T. Formation of volatile products during nitrate reduction on a Sn-modified Pt electrode in acid solution. *Journal of electroanalytical chemistry* **2011**, *662*, 87−92.

(31) Molodkina, E.; Botryakova, I.; Danilov, A.; Souza-Garcia, J.; Feliu, J. M. Kinetics and mechanism of nitrate and nitrite electroreduction on Pt (100) electrodes modified by copper adatoms. *Russian Journal of Electrochemistry* **2013**, *49*, 285−293.

(32) Molodkina, E.; Danilov, A.; Feliu, J. M. Cu UPD at Pt (100) and stepped faces Pt (610), Pt (410) of platinum single crystal electrodes. *Russian Journal of Electrochemistry* **2016**, *52*, 890−900.
(33) Kim, K.-W.; Kim, S.-M.; Kim, Y.-H.; Lee, E.-H.; Jee, K.-Y. Sn stability of Sn-modified Pt electrode for reduction of nitrate. *J. Electrochem. Soc.* **2007**, *154*, E145−E152.
(34) Elias, W. C.; Heck, K. N.; Guo, S.; Yazdi, S.; Ayala-Orozco, C.; Grossweiler, S.; Domingos, J. B.; Ringe, E.; Wong, M. S. Indium-decorated Pd nanocubes degrade nitrate anions rapidly. *Appl. Catal. B: Environmental* **2020**, *276*, 119048.
(35) Garnier, E.; VIDAL IGLESIAS, F. J.; Feliu, J. M.; Solla-Gullón, J. Surface structure characterization of shape and size controlled Pd nanoparticles by Cu UPD: a quantitative approach. *Frontiers in chemistry* **2019**, *7*, 527.
(36) Lim, J.; Liu, C.-Y.; Park, J.; Liu, Y.-H.; Senftle, T. P.; Lee, S. W.; Hatzell, M. C. Structure Sensitivity of Pd Facets for Enhanced Electrochemical Nitrate Reduction to Ammonia. *ACS Catal.* **2021**, *11*, 7568−7577.
(37) Kumar, A.; Buttry, D. A. Size-dependent underpotential deposition of copper on palladium nanoparticles. *J. Phys. Chem. C* **2015**, *119*, 16927−16933.
(38) Sundararaman, R.; Goddard, W. A., III; Arias, T. A. Grand canonical electronic density-functional theory: Algorithms and applications to electrochemistry. *J. Chem. Phys.* **2017**, *146*, 114104.
(39) Lu, X.; Song, H.; Cai, J.; Lu, S. Recent development of electrochemical nitrate reduction to ammonia: A mini review. *Electrochem. Commun.* **2021**, *129*, 107094.
(40) Wang, Y.; Zhou, W.; Jia, R.; Yu, Y.; Zhang, B. Unveiling the Activity Origin of a Copper-based Electrocatalyst for Selective Nitrate Reduction to Ammonia. *Angew. Chem.* **2020**, *132*, 5388−5392.
(41) Daiyan, R.; Tran-Phu, T.; Kumar, P.; Iputera, K.; Tong, Z.; Leverett, J.; Khan, M. H. A.; Asghar Esmailpour, A.; Jalili, A.; Lim, M.; Tricoli, A.; Liu, R.-S.; Lu, X.; Lovell, E.; Amal, R. Nitrate reduction to ammonium: from CuO defect engineering to waste NO x-to-NH 3 economic feasibility. *Energy Environ. Sci.* **2021**, *14*, 3588.
(42) Guo, S.; Heck, K.; Kasiraju, S.; Qian, H.; Zhao, Z.; Grabow, L. C.; Miller, J. T.; Wong, M. S. Insights into nitrate reduction over indium-decorated palladium nanoparticle catalysts. *ACS Catal.* **2018**, *8*, 503−515.
(43) Zhu, T.; Chen, Q.; Liao, P.; Duan, W.; Liang, S.; Yan, Z.; Feng, C. Single-Atom Cu Catalysts for Enhanced Electrocatalytic Nitrate Reduction with Significant Alleviation of Nitrite Production. *Small* **2020**, *16*, 2004526.
(44) Roy, C.; Deschamps, J.; Martin, M.; Bertin, E.; Reyter, D.; Garbarino, S.; Roué, L.; Guay, D. Identification of Cu surface active sites for a complete nitrate-to-nitrite conversion with nanostructured catalysts. *Appl. Catal. B: Environmental* **2016**, *187*, 399−407.
(45) Hörold, S.; Vorlop, K.-D.; Tacke, T.; Sell, M. Development of catalysts for a selective nitrate and nitrite removal from drinking water. *Catal. Today* **1993**, *17*, 21−30.
(46) Chun, H.-J.; Zeng, Z.; Greeley, J. DFT Insights into NO Electrochemical Reduction: A Case Study of Pt (211) and Cu (211) Surfaces. *ACS Catal.* **2022**, *12*, 1394−1402.
(47) Hara, K.; Kamata, M.; Sonoyama, N.; Sakata, T. Electrocatalytic reduction of NO on metal electrodes and gas diffusion electrodes in an aqueous electrolyte. *J. Electroanal. Chem.* **1998**, *451*, 181−186.
(48) Clark, C. A.; Reddy, C. P.; Xu, H.; Heck, K. N.; Luo, G.; Senftle, T. P.; Wong, M. S. Mechanistic Insights into pH-controlled nitrite reduction to ammonia and hydrazine over rhodium. *ACS catalysis* **2020**, *10*, 494−509.
(49) Huai, L.-y.; He, C.-z.; Wang, H.; Wen, H.; Yi, W.-c.; Liu, J.-y. NO dissociation and reduction by H2 on Pd (1 1 1): A first-principles study. *J. Catal.* **2015**, *322*, 73−83.
(50) Farberow, C. A.; Dumesic, J. A.; Mavrikakis, M. Density functional theory calculations and analysis of reaction pathways for reduction of nitric oxide by hydrogen on Pt (111). *ACS Catal.* **2014**, *4*, 3307−3319.
(51) Ma, H.; Li, S.; Wang, H.; Schneider, W. F. Water-mediated reduction of aqueous N-nitrosodimethylamine with Pd. *Environ. Sci. Technol.* **2019**, *53*, 7551−7563.
(52) McCalman, D. C.; Kelley, K. H.; Werth, C. J.; Shapley, J. R.; Schneider, W. F. Aqueous N2O Reduction with H2 over Pd-Based Catalyst: Mechanistic insights from experiment and simulation. *Top. Catal.* **2012**, *55*, 300−312.
(53) Akhade, S. A.; Bernstein, N. J.; Esopi, M. R.; Regula, M. J.; Janik, M. J. A simple method to approximate electrode potential-dependent activation energies using density functional theory. *Catal. Today* **2017**, *288*, 63−73.
(54) Ko, B. H.; Hasa, B.; Shin, H.; Zhao, Y.; Jiao, F. Electrochemical Reduction of Gaseous Nitrogen Oxides on Transition Metals at Ambient Conditions. *J. Am. Chem. Soc.* **2022**, *144*, 1258.
(55) Xie, X.; Gao, G.; Pan, Z.; Wang, T.; Meng, X.; Cai, L. Large-scale synthesis of palladium concave nanocubes with high-index facets for sustainable enhanced catalytic performance. *Sci. Rep.* **2015**, *5*, 8515.
(56) Xia, X.; Xie, S.; Liu, M.; Peng, H.-C.; Lu, N.; Wang, J.; Kim, M. J.; Xia, Y. On the role of surface diffusion in determining the shape or morphology of noble-metal nanocrystals. *Proc. Natl. Acad. Sci. U. S. A.* **2013**, *110*, 6669−6673.
(57) Jin, M.; Liu, H.; Zhang, H.; Xie, Z.; Liu, J.; Xia, Y. Synthesis of Pd nanocrystals enclosed by {100} facets and with sizes< 10 nm for application in CO oxidation. *Nano Research* **2011**, *4*, 83−91.
(58) Kresse, G.; Furthmüller, J. Efficient iterative schemes for ab initio total-energy calculations using a plane-wave basis set. *Phys. Rev. B* **1996**, *54*, 11169.
(59) Kresse, G.; Furthmüller, J. Efficiency of ab-initio total energy calculations for metals and semiconductors using a plane-wave basis set. *Computational materials science* **1996**, *6*, 15−50.
(60) Blöchl, P. E. Projector augmented-wave method. *Phys. Rev. B* **1994**, *50*, 17953.
(61) Kresse, G.; Joubert, D. From ultrasoft pseudopotentials to the projector augmented-wave method. *Physical review b* **1999**, *59*, 1758.
(62) Perdew, J. P.; Burke, K.; Ernzerhof, M. Generalized gradient approximation made simple. *Physical review letters* **1996**, *77*, 3865.
(63) Grimme, S.; Antony, J.; Ehrlich, S.; Krieg, H. A consistent and accurate ab initio parametrization of density functional dispersion correction (DFT-D) for the 94 elements H-Pu. *J. Chem. Phys.* **2010**, *132*, 154104.
(64) Monkhorst, H. J.; Pack, J. D. Special points for Brillouin-zone integrations. *Phys. Rev. B* **1976**, *13*, 5188.
(65) Methfessel, M.; Paxton, A. High-precision sampling for Brillouin-zone integration in metals. *Phys. Rev. B* **1989**, *40*, 3616.
(66) Henkelman, G.; Uberuaga, B. P.; Jónsson, H. A climbing image nudged elastic band method for finding saddle points and minimum energy paths. *J. Chem. Phys.* **2000**, *113*, 9901−9904.
(67) Henkelman, G.; Jónsson, H. Improved tangent estimate in the nudged elastic band method for finding minimum energy paths and saddle points. *J. Chem. Phys.* **2000**, *113*, 9978−9985.
(68) Henkelman, G.; Jónsson, H. A dimer method for finding saddle points on high dimensional potential surfaces using only first derivatives. *J. Chem. Phys.* **1999**, *111*, 7010−7022.
(69) McQuarrie, D. A.*Statistical Mechanics*; Sterling Publishing Company, 2000.
(70) Keith, J. A.; Carter, E. A. Theoretical insights into pyridinium-based photoelectrocatalytic reduction of CO2. *J. Am. Chem. Soc.* **2012**, *134*, 7580−7583.
(71) Valiev, M.; Bylaska, E. J.; Govind, N.; Kowalski, K.; Straatsma, T. P.; Van Dam, H. J.; Wang, D.; Nieplocha, J.; Apra, E.; Windus, T. L.; de Jong, W. NWChem: A comprehensive and scalable open-source solution for large scale molecular simulations. *Comput. Phys. Commun.* **2010**, *181*, 1477−1489.
(72) Nørskov, J. K.; Rossmeisl, J.; Logadottir, A.; Lindqvist, L.; Kitchin, J. R.; Bligaard, T.; Jonsson, H. Origin of the overpotential for oxygen reduction at a fuel-cell cathode. *J. Phys. Chem. B* **2004**, *108*, 17886−17892.

https://doi.org/10.1021/acscatal.2c04841
ACS Catal. 2023, 13, 87−98

(73) Speight, J. G.*Lange's Handbook of Chemistry*; McGraw-Hill: New York, 2005; Vol. *1*.
(74) Chance, B.; Devault, D. C.; Frauenfelder, H.*Tunneling in Biological Systems: A Colloquium of the Johnson Research Foundation*; Academic Press, 2013.
(75) Perrin, D. D.*Ionisation Constants of Inorganic Acids and Bases in Aqueous Solution*; Elsevier, 2016.

https://doi.org/10.1021/acscatal.2c04841
ACS Catal. 2023, 13, 87−98